Experimental study of damping enhancement in aluminum rods by knurling

Suparno Bhattacharyya*[1] and Anindya Chatterjee[2]

[1]Institute of Data Science, Texas A&M University, College Station, TX, USA
[2]Department of Mechanical Engineering, Indian Institute of Technology Kanpur, India

Abstract

This paper is motivated by an interest in the damping behaviour of lightly damped metal components. Some anecdotal evidence suggests that near surface plastic deformation, such as in shot peening, might increase the damping of metallic components. Here we have studied the damping behaviour of slender aluminum rods in the first free-free mode, suspended at a nodal point. Three types of rods were studied: a plain rod, a knurled rod, and a plain rod wrapped with viscoelastic tape. Two rods of each type were tested. Free vibration responses of the struck rods were measured and recorded after analog and digital filtering. Damping coefficients were determined from ten measurements per rod. Results were consistent within each rod pair but significantly differed across rod types. Knurled rods exhibited approximately 1.6 times the damping of plain rods, while viscoelastic tape increased damping by a factor of 2.3. The possible role of surface roughness-induced air damping for knurled rods was investigated analytically as well as numerically (using FLUENT). It was concluded that air damping effects were

---

*Corresponding author (suparno.bhattacharyya@gmail.com)

weak; and that knurling, which is a near-surface deformation process, can significantly increase the damping in metal components. Although the increase is lower than it is with viscoelastic damping layers, near-surface deformation induced damping may be preferred in some applications.

Keywords: Dissipation, damping coefficient, hysteresis, dislocation density, knurling

1 Introduction

Deformation in vibrating solids is accompanied by energy dissipation. This dissipation is referred to as damping, a critical characteristic in engineering materials. Unwanted vibrations in engineering components can cause detrimental effects, particularly in metal components excited near their natural frequencies. Without adequate damping, even minor disturbances can potentially result in large amplitude oscillations. In automotive parts, for example, excessive vibrations may cause noise, poor ride quality, structural damage, and reduced life. Consequently, the study of damping characteristics and the enhancement of damping properties in engineering materials has long been a topic of research.

Various damping mechanisms exist in mechanical systems, including but not limited to viscous damping, eddy current damping, Coulomb damping, and material damping. This paper focuses on material damping. Material damping is primarily attributed to energy dissipation associated with microstructural defects such as dislocations, grain boundaries, and impurities within the material [1]. During vibrations, movement of dislocations induce internal friction, which results in energy loss during each stress cycle. The Granato-Lücke theory [2] is a classical model used to describe material damping due to dislocations in crystalline materials. The theory proposes that dislocations, acting as string-like entities, are pinned at points along their length by point defects. When the material is subjected to a cyclic stress, these dislocations can bow out between pinning points, dissipating vibrational energy. This energy dissipation is manifested as material damping. The stress-strain relationship for a vibrating element due to this type of damping typically displays a hysteresis loop, where the loop's area represents the energy dissipated per cycle [3].

Considering that material damping is affected by microstructural defects and their interactions, it is reasonable to assume that an increase in the number of dislocations could improve the damping capacity of the material. Since plastic deformations generate new dislocations in metals, such deformations might enhance the damping characteristics of metals.

A few studies in this general area have already been conducted. For instance, the enhancement of damping in aluminum-matrix composites through the addition of graphite and silicon carbides was examined in [4]. Chung's review on materials for vibration damping [5] includes an experimental study involving metals, polymers, and ceramics aimed at reducing vibrations in structures. He concluded that "damping enhancement in metals is predominantly a matter of microstructural design." Nevertheless, except for [6], [7], and [8], there appears to be limited literature providing direct insight into the effect of deliberate near-surface plastic deformations on the damping of metals. In [7], the authors examined how cold working affects the correlation between internal friction (within the vibrating continuum) and strain amplitude at low temperatures. Additionally, the influence of shot peening and sand blasting on the damping properties of steel has been studied in [6] and [8]. In [6], the authors showed experimentally that shot peening increased the damping factor in 304 austenitic stainless steel, with a linear relationship observed between the damping factor and the depth of the deformed layer. More recently, in Ref. [9], the authors examined the influence of tool rotational speed on the damping capacity of Friction Stir processed [10] pure aluminum. They found that lower tool rotational speeds (600 rpm) produced finer grain structures and higher damping capacities, especially at elevated temperatures.

These findings corroborate our previously hypothesized correlation between plastic deformation and damping in metals. To investigate further, in this work, we analyzed the effect of a near-surface plastic deformation process, namely knurling, on the damping characteristics of aluminum components. Knurling, as a process, is more straightforward in comparison to friction stir processing and shotpeening for slender rods and easily achieved using lathes. We evaluated the damping properties of several aluminum rods, both with and without knurling, through experimental and related analysis to determine if the process significantly affects their damping characteristics.

The potential influence of air damping on the vibrating components was also considered, as it could have conceivably enhanced damping because of the roughening of the surface of the rod due to knurling. This factor was accounted for, and air damping was estimated using a theoretical simulation that provides academic support for the main empirical observation of this paper. The results demonstrated that air damping was not the primary factor responsible for the observed increase in damping. Consequently, it was concluded, that like the other few surface deformation processes referred to above, knurling also significantly enhances damping in metals.

2 Experimental study of damping in aluminum rods

In our experiments, we estimated and compared the damping coefficients associated with the first free-free mode of vibration of several aluminum rods. Employing the free-free mode (experimental setup detailed later) minimized the influence of boundary damping effects [11] so that the observed energy losses can only be attributed to internal material damping and possibly to the surrounding air. During the experiments, each rod was lightly struck to induce vibration, and the resulting vibrational response was recorded using a strain gauge and data acquisition system. From the recorded data, the time series corresponding to the first mode of vibration was extracted, to estimate the damping coefficients.

In this section we discuss the equipment used, the experimental setup, some design considerations, and the procedure followed during the experiment.

2.1 Equipment

Elements	**Weight (%)**
C	2.34
O	1.21
Mg	0.27
Al	95.36
Si	0.51
Fe	0.31
Total	**100**

Table 1: Elemental composition of one of the aluminum rod obtained from Energy-dispersive X-ray spectroscopy. The analysis was conducted at the Scanning Electron Microscopy facility, Corrosion Laboratory, Department of Materials Science and Engineering, IIT Kanpur.

The aluminum rods used in this experiment were sourced from the same batch and were purchased off-the-shelf from a local hardware store at the same time. The chemical composition of one such rod is tabulated in Table 1. A total of six rods were used, each with a length of 834 mm and a diameter of 11.5 mm. The rods were categorized as follows: two plain rods, two rods with knurling over 400 mm of their length (diamond patterned, applied using the same lathe-mounted knurling tool on both rods), and two plain rods with visco-elastic tape wrapped around their surface over a length equal to the knurling. One rod of each type is shown in Fig. 1. The third type of rod was included to compare with an actual damping treatment. Each rod had two 4 mm diameter holes drilled at a distance of 187 mm from each end (see Fig. 2). The design aspects of the rods are further discussed in Section 2.2.

Strain gauges of type FLA 5-11 (120 Ω, gauge factor 2.11) were used to record the deformation of the vibrating rods. The data were acquired using a National Instruments CompactDAQ 4-Slot Ethernet Chassis with an NI 9215 module, while the analysis of the acquired data was performed using MATLAB. The electronic equipment included resistances, trimpots, capacitors, breadboards, IC-741CN, IC-TL084, IC-7805, and 9V batteries.

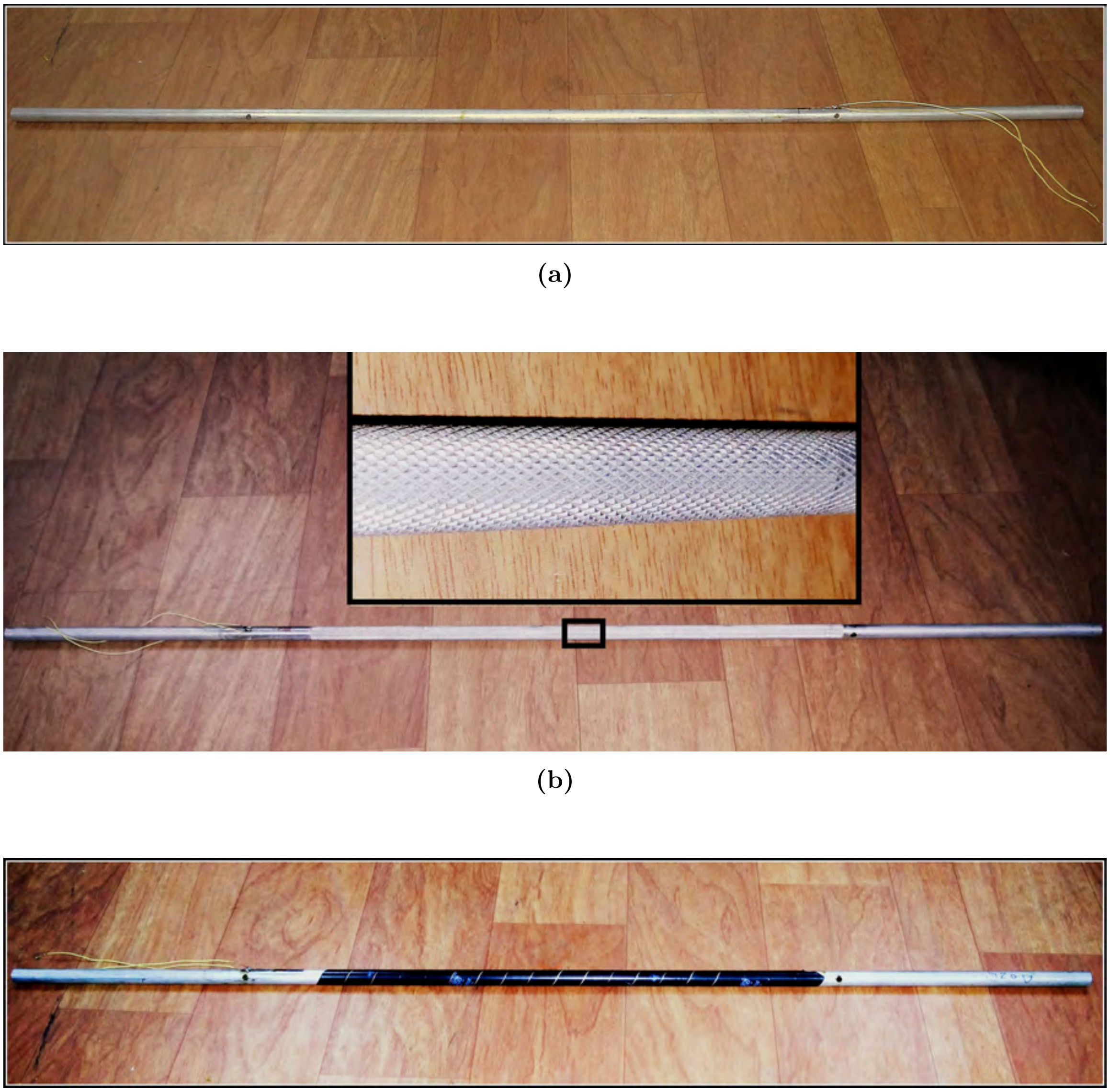

(a)

(b)

(c)

Figure 1: Photographs of the different types of aluminum rods used in the experiment: (a) plain rod, (b) knurled rod (inset showing the knurled texture), and (c) rod partially wrapped with visco-elastic tape.

2.2 Design considerations

As mentioned above, we estimated and compared the damping coefficient values of six aluminum rods in the first free-free mode of vibration. Some details follow.

2.2.1 Geometry of the aluminum rods

All six rods used had identical dimensions, with a first natural frequency of approximately 75 Hz. This frequency was distant from the power supply frequency, which led to lower measurement noise. The natural frequency calculations were conducted using the modal analysis module in ANSYS, as well as analytical methods (see Appendix A) using the Euler-Bernoulli beam model.

2.2.2 Support configuration

During the experiment, each rod was suspended from a knife-edge support passing through one of the two 4 mm holes (away from the strain gauge) that were drilled at a distance of 187 mm from the ends. This support condition was chosen so that the line of contact between the knife-edge and the inner surface of the drilled hole aligned with the *nearby node* (Fig. 2), which ensured minimal movement of the rod near the support, thereby eliminating Coulomb damping during vibration. To further facilitate the excitation of the first mode, alongwith this support configuration, the rods were also struck near the midspan, as the displacement in the first mode is large at the midspan. The location and intensity of the excitation remained consistent (to within an acceptable tolerance) across all rods. Such an arrangement also prevented excitation of the higher modes.

In this configuration, though one hole was sufficient for suspension, the other hole was drilled to maintain the symmetry of the system. A 3D elastodynamics simulation in ANSYS further confirmed that drilling 4 mm holes did not significantly affect the position of the nodes (Fig. 3b) of the beam. Note that connecting the strain gauge wires at the other node helped to damp higher modes due to movement of the wires, but left the first mode unaffected.

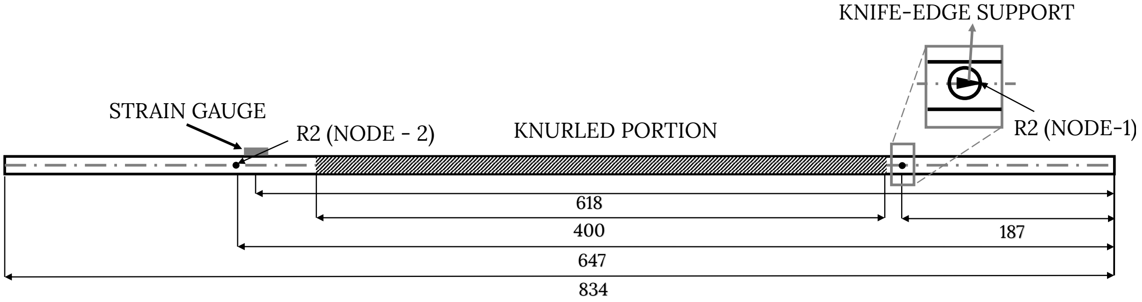

Figure 2: Geometric details and dimensions of the knurled rod used in the experiment. The hatch lines indicate the knurled texture. Except for the knurled portion, the geometric features of this rod are identical to that of the plain and the taped rods. Hence, separate schematics of the latter two types are not provided. All dimensions are in millimeters (not to scale). During the experiment the rods were suspended vertically from the hole at Node 1, i.e., away from the strain gauge wires.

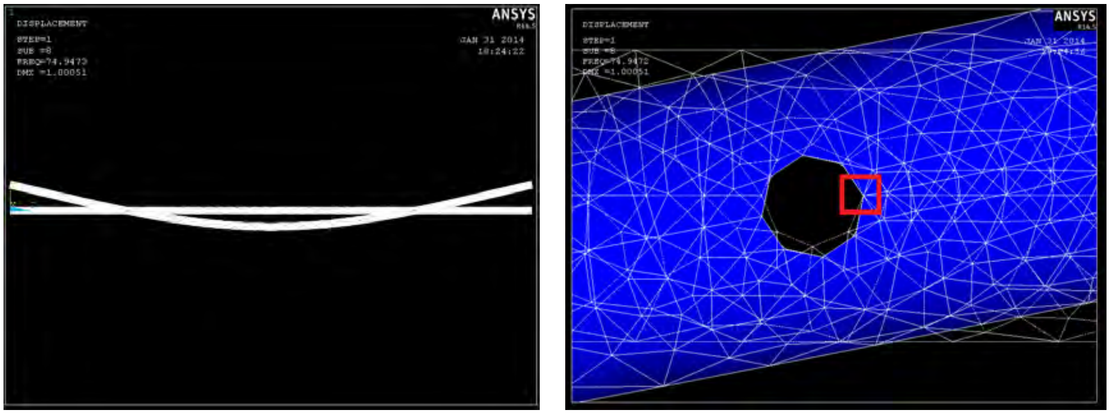

(a) **(b)**

Figure 3: Modal analysis of the alumnium rod in ANSYS, featuring: (a) the mode shape corresponding to the first natural frequency under free-free boundary conditions, and (b) the unchanged spatial location of the node (marked red) in both the deformed (blue wireframe) and undeformed (transparent wireframe) configurations of the rod, despite the 4 mm diameter holes. The analysis used SOLID187 elements and Block Lanczos method.

2.2.3 Minimizing rigid body oscillation

To control the rigid body (or pendulum-like) oscillation of the vertical test rod following an initial strike, an additional horizontal rod was placed near the second nodal point of the vertical rod (see Fig. 4). This horizontal rod was free to rotate about a vertical axis

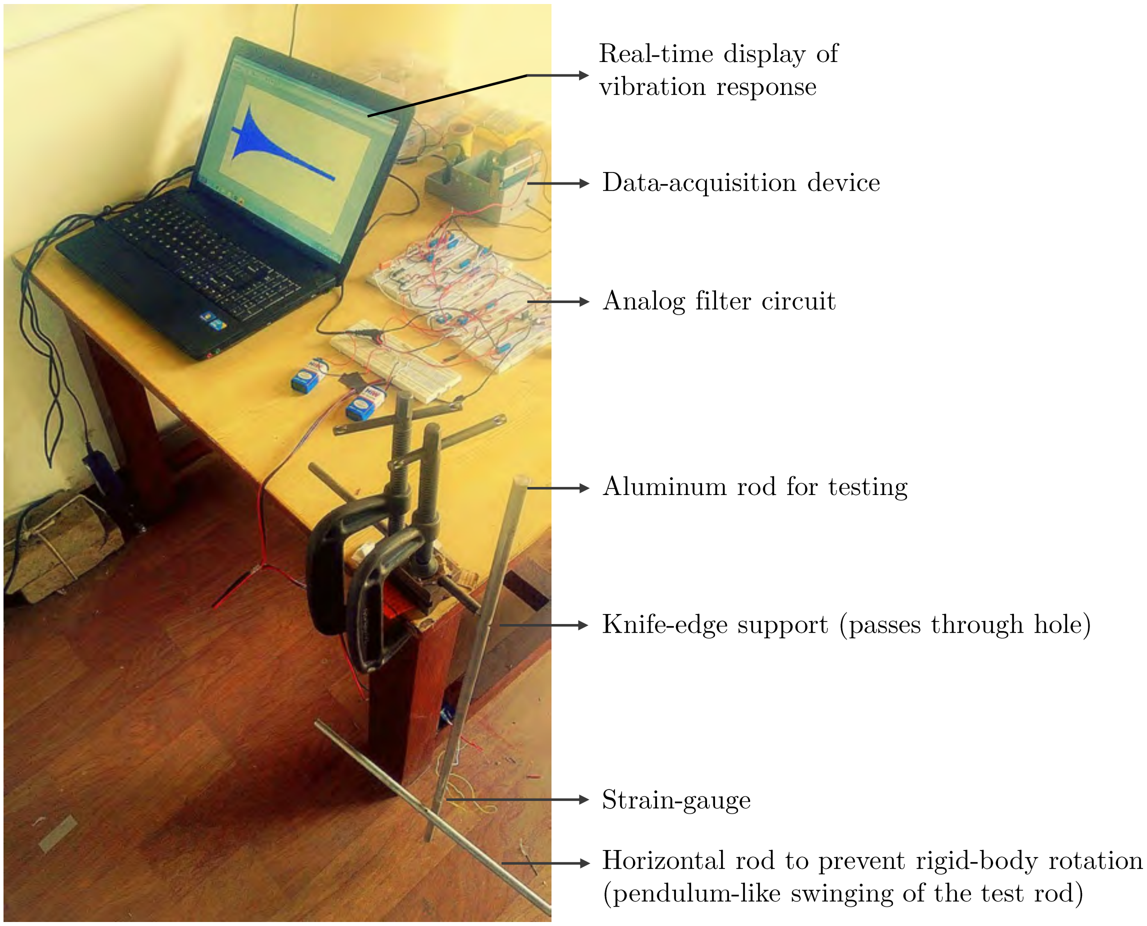

Figure 4: The experimental setup.

and served to dissipate much of the energy associated with the rigid body oscillation of the vertical rod after impact. This step further lowered the unwanted motion of the wires connected to the strain gauge. The horizontal rod's impact at the lower *nodal* point of the test rod prevented unintended attenuation of the first mode response.

2.2.4 Positioning of the strain gauge

As mentioned above, a strain gauge on each rod was positioned near the second nodal point, away from the support point (see Fig. 2). Wires from the gauge were soldered to another terminal mounted on the rod. Fine external wires with very low inertia were soldered to this terminal and were connected to a *Quarter Bridge* circuit. The placement of the gauge and the terminal near the nodal point ensured that a negligible fraction of the first mode vibrational energy would get transferred to wires.

2.2.5 Circuit design for signal amplification and noise attenuation

In the absence of large amplitude oscillation and deformation of the rods, the strain amplitude remains low, resulting in a weak signal from the strain gauge. Amplifying the signal was necessary. In the first stage a differential amplifier, with a gain factor of 100, was used for preliminary amplification of the signal. However, the 50 Hz noise (supply frequency) mixed in the acquired signal needed to be eliminated before the signal could be further amplified. Hence, another circuit was constructed (refer to Figs. 5 and 6), which included a notch filter to eliminate the 50 Hz noise, followed by a bandpass filter centered close to the rod's first natural frequency, followed by two amplifiers, each with a gain factor 5, leading to a total gain of approximately 10^4. The filtered and amplified signal coming out of this circuit was then fed into a data acquisition (DAQ) system, a National Instruments *CompactDAQ 4-Slot Ethernet Chassis* with *NI 9215 module*, which was connected to a computer via a USB cable. The vibrational responses were recorded and stored on the computer using MATLAB via its DAQ-interface.

2.3 Experimental procedure

Each rod was given an impulse at the midpoint with a small aluminum striker. Following initial excitation, the analog-filtered vibration signal was acquired through the DAQ system at a sampling frequency of 2048 Hz for 150 seconds and was recorded in MATLAB through its inbuilt data acquisition toolbox. Data were collected from two rods of each type: plain, knurled, and taped. Since all rods were sourced from the same batch at the same time, their average behavior was expected to be the same. With surface treatment being the only

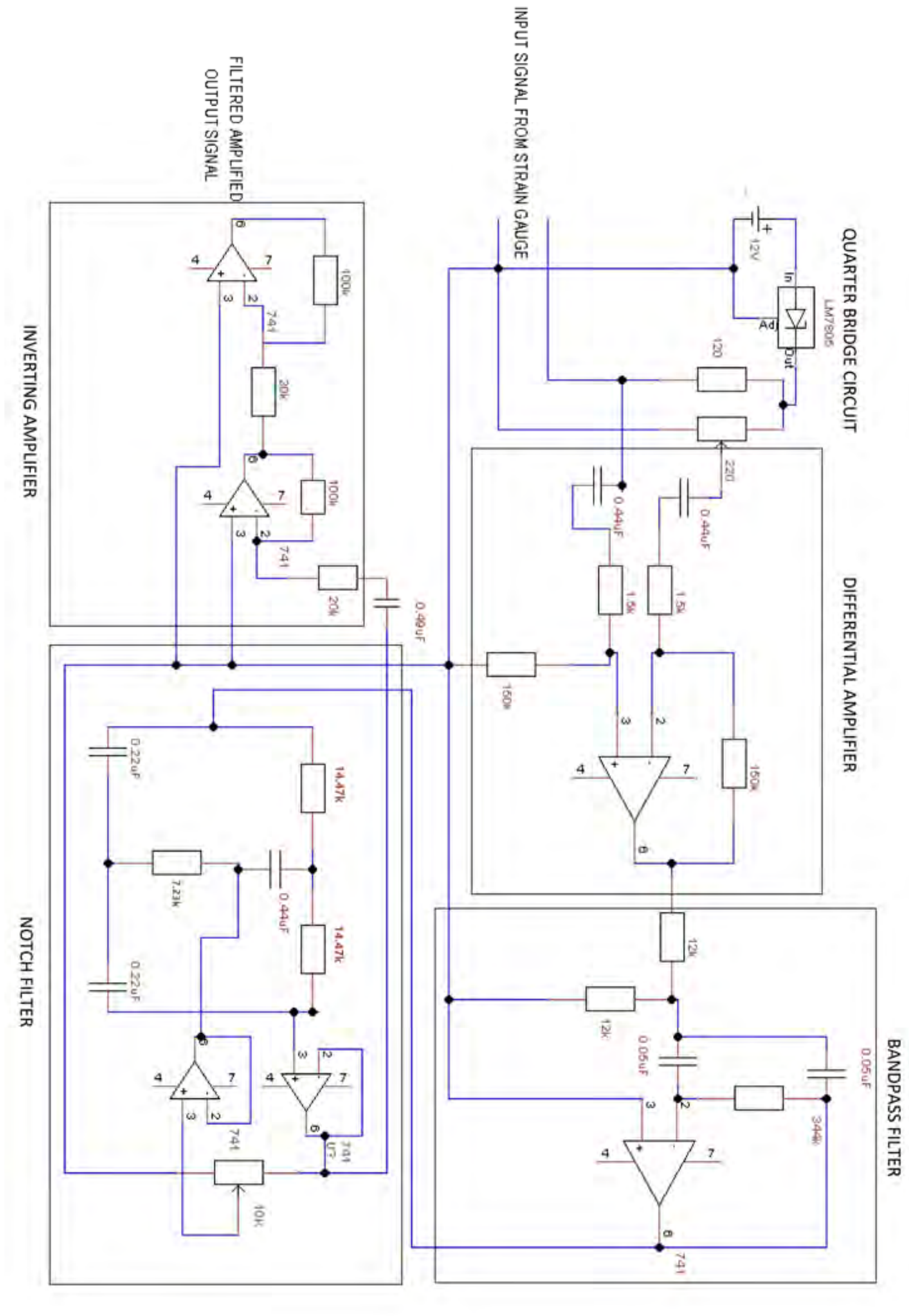

Figure 5: Schematic of the signal amplification and noise filtration circuit, comprising five sections: quarter bridge circuit, differential amplifier, bandpass filter, notch filter, and inverting amplifier. The quarter bridge circuit provides the strain measurement, to be amplified by the differential amplifier. The bandpass filter attenuates signals far from 75 Hz (first free-free mode), and the notch filter strongly attenuates the 50 Hz line frequency. The inverting amplifier adjusts signal polarity and provides additional amplification.

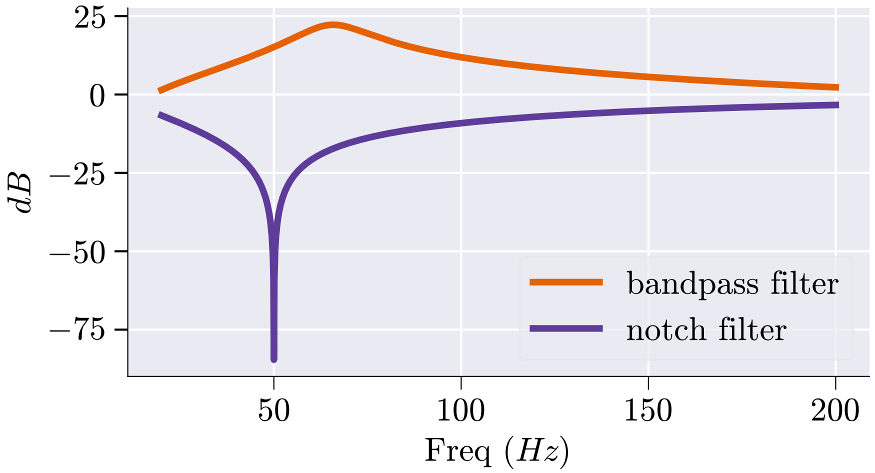

Figure 6: Computed frequency response (amplitudes) of the notch and the bandpass filters. Given our interest in the first natural frequency of the rod (75 Hz), the response curve of the bandpass filter was required to be fairly high at this frequency, but not necessarily flat across the adjacent range.

distinguishing factor, two rods per type were deemed adequate for analysis. Nonetheless, multiple runs per rod were performed to ensure sufficient data for meaningful statistical analyses. Specifically, ten readings were taken for each of these six rods, yielding a total of sixty time-series datasets.

The collected data was again filtered, this time using a *digital* bandpass filter designed in `MATLAB` for further noise reduction. A finite impulse response (FIR) bandpass filter [12] was employed for this purpose. The filter order was chosen to prevent any significant amplitude distortion, and `MATLAB`'s `filtfilt` function was used to eliminate phase distortion. The filter exhibited a sharp cutoff outside the passband, while maintaining a frequency response amplitude close to unity within the passband, thereby minimizing distortion. On the left column of Fig. 7, we present a representative dataset acquired from the three types of rods (plain on the top, knurled in the middle, and taped at the bottow row) that has been filtered and amplified using the analog filter circuit described in Section 2.2.5, whereas on the right, we show the processed and cleaned data obtained after the digital filtering. The damping coefficients for each aluminum rod were subsequently estimated from the final processed and cleaned data, as discussed in the next section.

3 Damping estimation from observed data

Direct visual inspection of the time series in Fig. 7 reveals a gradual increase in the rate of decay across the signals, with the progression moving from the plain (Figs. 7a and 7b) to the knurled (Figs. 7c and 7d), and finally to the taped rods (Figs. 7e and 7f). This same progression was observed in other datasets as well.

To quantify this trend, we numerically estimated the damping across multiple experiments for each rod type. In the absence of a dedicated theoretical damping model for this particular problem, polynomial fits were used to quantify the amplitude decay rate and compare the three rod types. A Quadratic and a cubic damping model were initially evaluated to estimate the damping coefficients, with higher-order terms to capture potential nonlinear dependence on amplitude. Subsequently, the cubic model was finally adopted. The details of both models and the parameter estimation techniques used in the analysis are provided below.

3.1 Quadratic model of damping

We initially considered the following quadratic model to estimate the rate of decay of the oscillation amplitude:

$$\frac{dA(t)}{dt} = -a_1 - a_2 A(t) - a_3 A^2(t) \tag{1}$$

where $A(t)$ is the averaged oscillation amplitude, decaying over time and measured in volts (V). The symbols a_1, a_2, and a_3 represent the coefficient of dry friction ($\mathrm{V\,s^{-1}}$), linear ($\mathrm{s^{-1}}$), and nonlinear damping ($\mathrm{V^{-1}\,s^{-1}}$), respectively. Solving Eq. (1) for t (calculated in

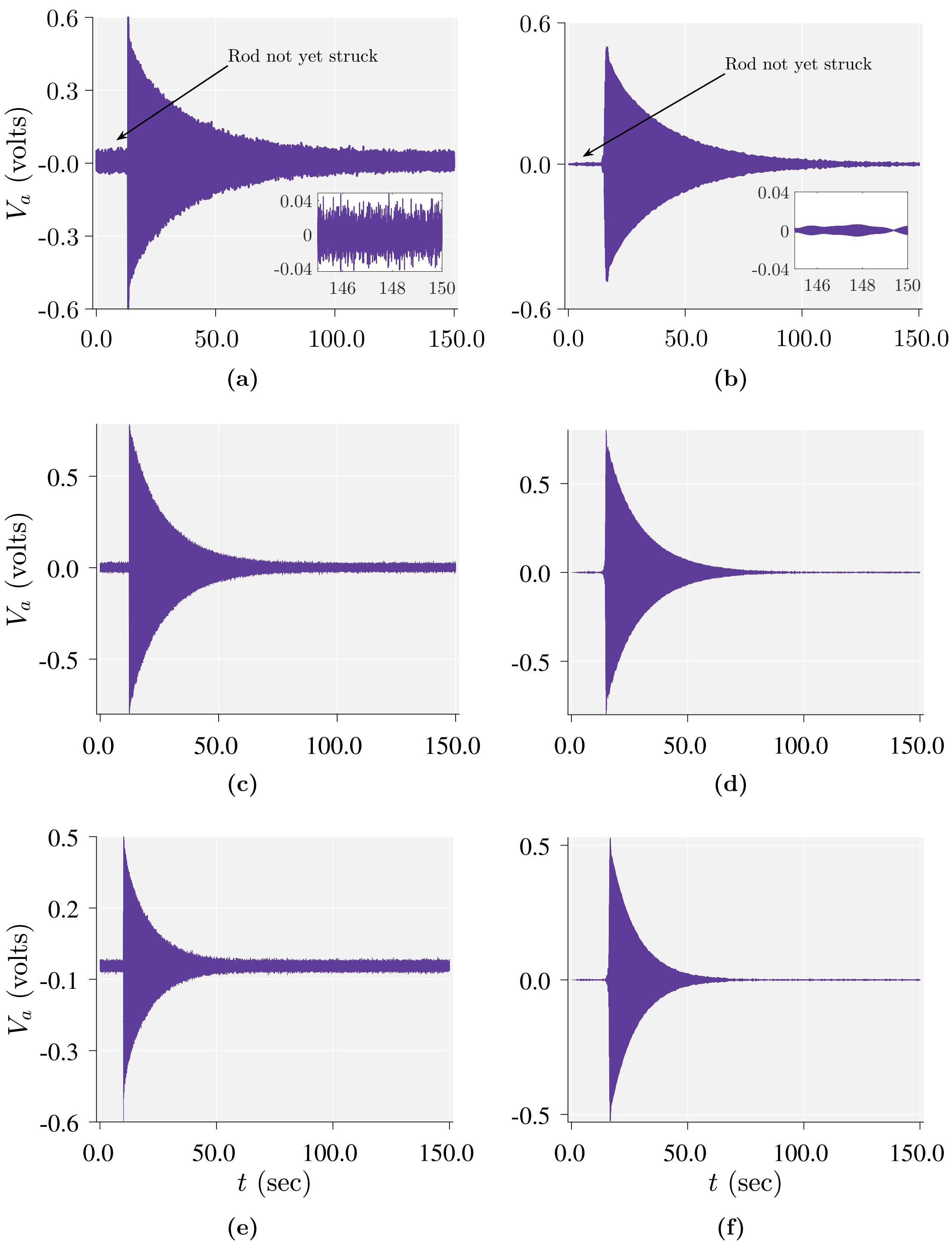

(a) **(b)** **(c)** **(d)** **(e)** **(f)**

Figure 7: Representative time-series data processed with analog filters (left column) and corresponding digitally filtered (right column) data for the first mode of vibration of a plain aluminum rod (a-b), a knurled aluminum rod (c-d), and a rod partially wrapped with viscoelastic tape (e-f). The symbol V_a for the three snapshots on the left represents the final amplified signal in Volts, as recorded by the data acquisition device. Note that the plots in each row share the same y-label, while the plots in each column share the same x-label.

`MAPLE`) we obtain

$$t = \begin{cases} \left(\operatorname{arctanh}\left(\frac{2a_3A_0+a_2}{\sqrt{-4a_1a_3+a_2^2}}\right) - \operatorname{arctanh}\left(\frac{2A(t)a_3+a_2}{\sqrt{-4a_1a_3+a_2^2}}\right)\right)\frac{1}{\sqrt{-4a_1a_3+a_2^2}}, \\ \qquad \text{if } 4a_1a_3 - a_2^2 < 0, \\ 2\left(\arctan\left(\frac{2a_3A_0+a_2}{\sqrt{4a_1a_3-a_2^2}}\right) - \arctan\left(\frac{2A(t)a_3+a_2}{\sqrt{4a_1a_3-a_2^2}}\right)\right)\frac{1}{\sqrt{4a_1a_3-a_2^2}}, \\ \qquad \text{if } 4a_1a_3 - a_2^2 > 0. \end{cases} \tag{2}$$

where A_0 is the initial amplitude of vibration (at time $t = 0$).

We estimated the parameters of Eq. (1) for the experimental data obtained from the three types of rod. As mentioned earlier, the total dataset included 60 time series (10 each, from two rods each, of three types of rods). For each time series, a segment of the decaying response was selected where the amplitudes ranged between 80% and 20% of the maximum amplitude. Data points from the upper half of the decay envelope within this segment were extracted using `MATLAB`'s `findpeaks` command [13, 14]. Subsequently, Eq. (1) was fitted to these points, and the parameters a_1, a_2, and a_3 were determined using `MATLAB`'s built-in optimization algorithm `fminsearch`. This is demonstrated in Fig. 8, where the orange envelope in the plots on the left column show data selected for parameter estimation for the plain, knurled, and taped beams (top, middle, and bottom rows, respectively). Plots on the right column show the scatter plot of the selected envelope in orange and the fitted curve in purple.

The mean and the standard deviations of the estimated parameters from the various experiments are presented in Table 2. For each rod type, parameter values were consistent across rod pairs, as indicated by the low standard deviation. Thus, we report parameter values for rod types only, rather than for individual rods.

It is evident that the coefficient of dry friction damping, a_1, is significantly smaller in all

Table 2: Coefficients obtained from the damping model provided in Eq. (1) for different types of rods. The table includes the mean (μ) and standard deviation (σ) of the coefficient of dry friction damping (a_1), the coefficient of linear damping (a_2), and the coefficient of the quadratic term (a_3).

Type	μ_{a_1} ($\pm\sigma_{a_1}$), (Vs^{-1})	μ_{a_2} ($\pm\sigma_{a_2}$), (s^{-1})	μ_{a_3} ($\pm\sigma_{a_3}$), (V^{-1}s^{-1})
Plain rod	9.4241×10^{-5} ($\pm 1.3351 \times 10^{-4}$)	0.0379 ($\pm$0.0022)	0.0122 ($\pm$0.0066)
Knurled rod	9.6259×10^{-5} ($\pm 2.0315 \times 10^{-4}$)	0.0618 ($\pm$0.0035)	0.0236 ($\pm$0.0084)
Rod with visco-elastic tape	1.4143×10^{-4} ($\pm 1.9368 \times 10^{-4}$)	0.0857 ($\pm$0.0038)	0.0506 ($\pm$0.0052)

cases, across all types of rod, compared to the other parameters. This outcome, however, is expected since (a) the strain associated with the vibration was minimal, approximately 10^{-5}, and (b) the support configuration of the rod was specifically designed to mitigate frictional damping during oscillation, as described in Section 2.2.2. Consequently, we dropped a_1 and reevaluated the damping coefficients using a second mathematical model.

3.2 Model without dry friction

$$\frac{dA(t)}{dt} = -a_2 A(t) - a_3 A^3(t), \tag{3}$$

Equation (3) describes a simpler damping model, which excludes the dry friction coefficient a_1. We incorporated a cubic term in Eq. (3) in place of the quadratic term used in Eq. (2). The rest of the symbols bear the same meaning as before. The solution to Eq. (3) is given by:

$$A(t) = \pm \left(e^{2a_2 t} \left(A_0^{-2} + \frac{a_3}{a_2} \right) - \frac{a_3}{a_2} \right)^{-\frac{1}{2}} \tag{4}$$

We re-estimated the parameters in Eq. (4) for the same experimental dataset, consisting of 60 time-series, employing the same estimation method as before. The coefficients a_2 and a_3, are plotted in Fig. 9. This rain-cloud plot provides consolidated information on the data distribution, as well as summary statistics for each dataset.

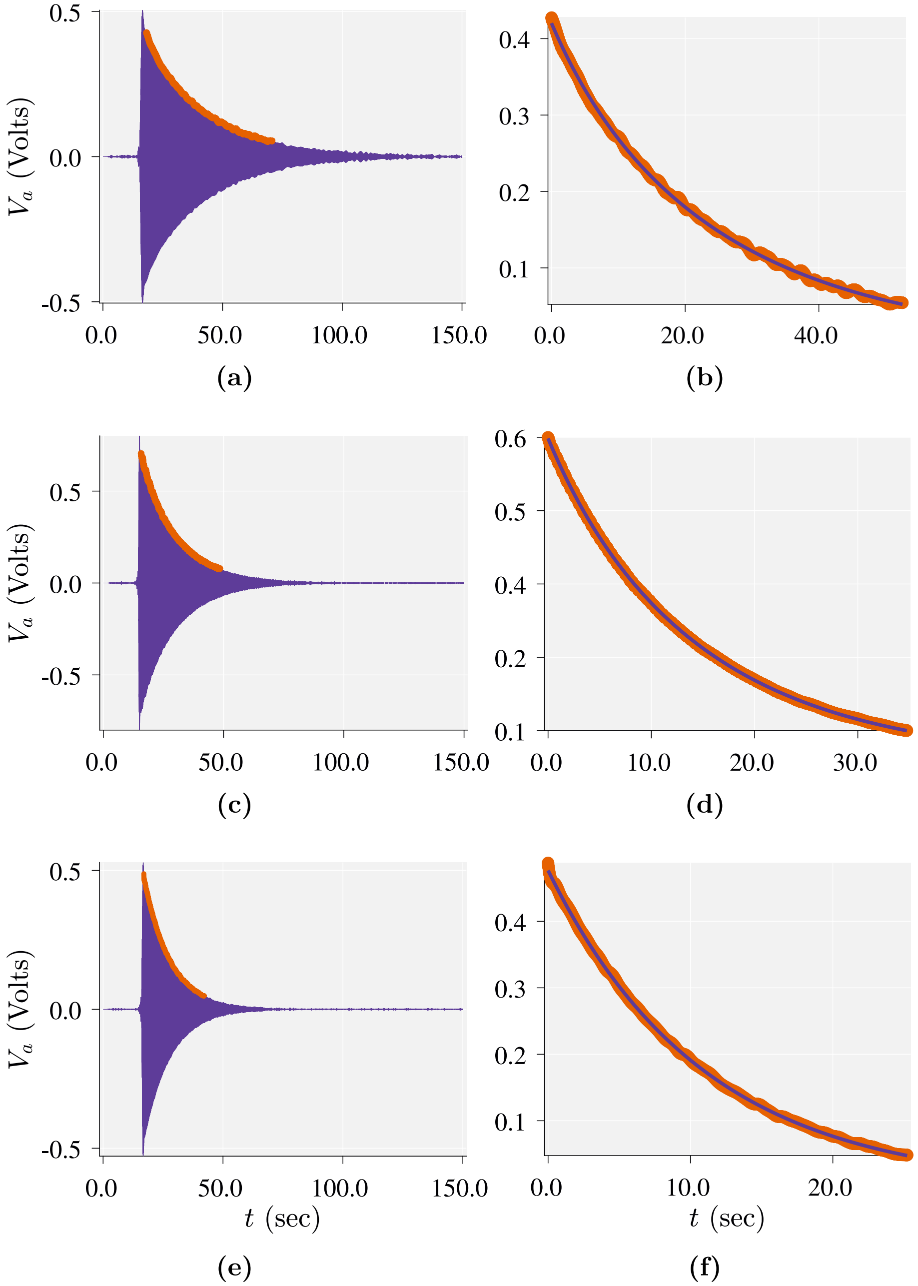

Figure 8: Data sets used for estimating the decay rate of vibration amplitude for three representative cases. All three datasets in the left column correspond to the filtered outputs in the right column of Fig. 7. The orange datasets, which captures the envelope of each decaying time series, indicate the portion used for estimating the coefficients of rate of decay in Eq. (4). On the right column, the orange datasets are shown in isolation along with their respective fitted curves obtained using Eq. (4). As in Fig. 7, the plots in each row share the same y-label, while the plots in each column share the same x-label.

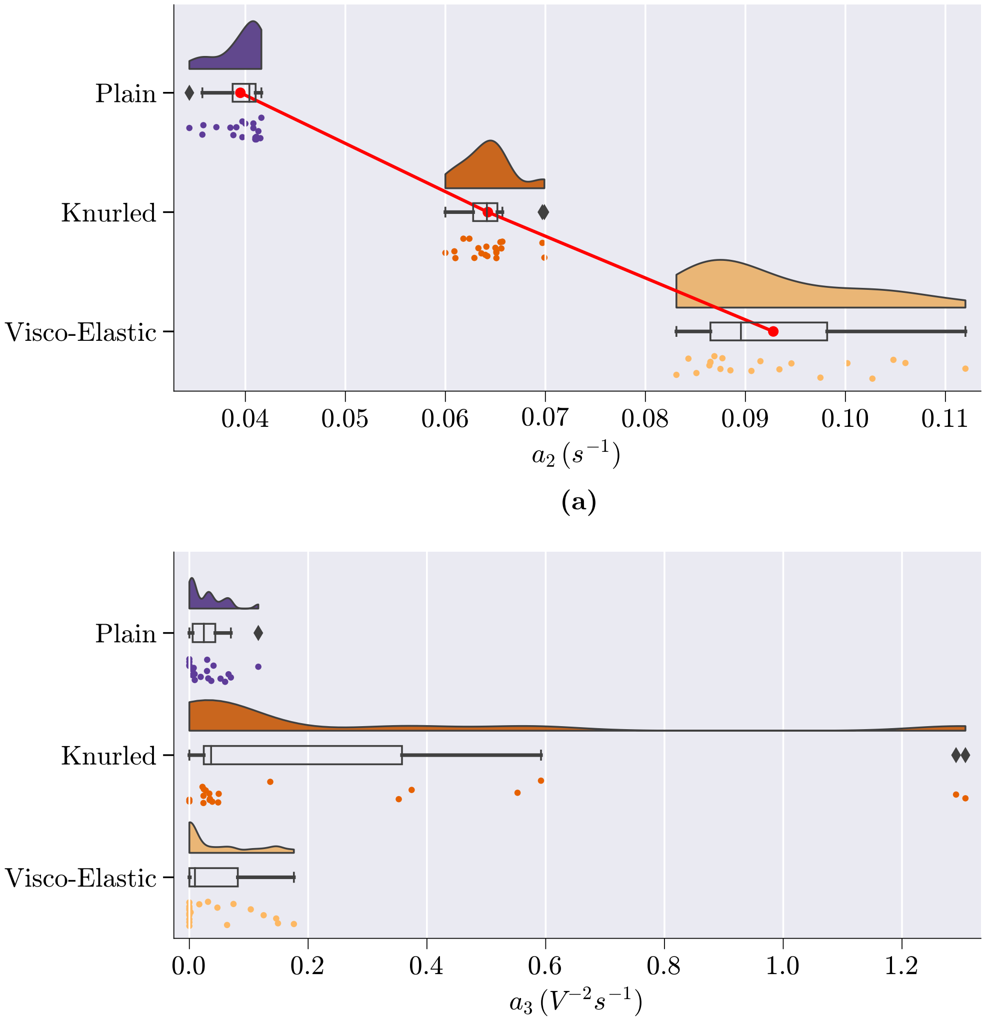

(a)

(b)

Figure 9: Rain cloud plots [15] depicting the distribution of damping coefficients in Eq. (4) derived from the experimental data obtained for three types of rods: plain (purple), knurled (orange), and those partially wrapped with visco-elastic tape (yellow). For each rod type, two identical rods were tested ten times, resulting in twenty data points. (a) The distribution of linear damping coefficients across the three rod types, highlighting that on average, knurled rods exhibit a significantly higher linear damping coefficient—approximately 1.6 times that of plain rods. (b) The distribution of the cubic damping coefficients, which exhibits more variability, with less discernible patterns.

As seen from Fig. 9a, the mean value (marked using red dot) and the distribution of the linear damping coefficients clearly show a steady increase from plain to knurled to taped rods. Specifically, the mean value of a_2 for the knurled aluminum rods was found to be almost *1.6 times that of plain rods*: 0.0642 s^{-1} ($\sigma_{a_2} = 1.5 \times 10^{-3}$) compared to 0.0395 s^{-1} ($\sigma_{a_2} = 10^{-3}$), whereas the mean a_2 for the taped rod was found to be 0.0928 s^{-1} ($\sigma_{a_2} = 5 \times 10^{-3}$) .

In contrast to a_2, the coefficient of the cubic term a_3 does not exhibit a discernible trend, as seen from the distribution in Fig. 9b. For both the plain and viscoelastic cases, a_3 falls within the range of [0, 0.2] $\mathrm{V}^{-2}\mathrm{s}^{-1}$, with most values clustered near 0. This pattern holds for the knurled rods as well, although in a few instances (6 out of 20), higher values of a_3 were observed.

Our primary focus lies in the behavior of the exponential decay at smaller amplitudes, where the contribution of the cubic term and its coefficient is expected to be negligible. However, we note that the amplitudes of the first few data points on the envelope selected for fitting the damping model were nearly 80% of the excitation amplitude, which influenced the contribution of the cubic term, particularly in cases where the excitation amplitude was relatively high. We suspect this is the reason behind the larger values of a_3 observed.

One key challenge encountered during the experiment stemmed from the axisymmetry of the rods, which gave rise to two modes corresponding to the same natural frequency. These modes can exchange energy and exhibit nonlinear interactions [16, 17], particularly under large initial excitation. However, at lower excitation levels, this effect becomes less significant. In cases of large-amplitude excitation, this phenomenon occasionally induced sideways rocking oscillations and rattling motion near the knife-edge support. In some datasets, this was reflected as an initial non-exponential decay rate, which later transitioned into a slower exponential decay. Fig. 10 illustrates one such time-series.

Nevertheless, due to the system's nearly linear behavior at lower amplitudes, the decay rate could be well approximated using Eq. (4). In these cases, we identified the segment of the time series where the decay was nearly exponential, as indicated by the orange portion in Fig. 10, to estimate the damping coefficients. Most datasets, however, did not exhibit pronounced non-exponential behavior, and the majority were consistent, enabling a reliable estimation of the decay rate.

4 Estimation of air damping

Our experiments were carried out in air. Hence, it was important to check if apart from internal damping, air damping might also play a role in the increase of damping. It is expected that for the low vibration frequencies involved, damping due to radiated acoustic energy will be negligible. The analysis is classical, in the flavor of [18], and routine. For completeness, an outline is provided in Appendix C, where the dissipation due to air viscosity is also estimated analytically. Additionally, an estimation of the dissipation due to viscosity was carried out in FLUENT [19] as well and is discussed below. FLUENT also enabled analyzing the effect of the local viscous forces at the knurled (non-smooth) surface, potentially contributing to additional energy dissipation.

In FLUENT, we simulated the oscillation of the two-dimensional model of the cylinder. The model was treated as a bounded circular region with a radius equal to that of the cylinder, with fluid flowing in a square domain outside this region. To simulate the cylinder's oscillation, a periodic velocity boundary condition (for $\omega = 75$ Hz and maximum displacement $= 0.001$ m) was applied. The outlet pressure on the outer boundaries was set to zero. Using the simulation data, we compared the maximum shear stress value induced at the boundary of the circular region with our theoretical results in Appendix C.

The FLUENT simulation predicted a maximum shear force ($\tau_{\max}$) of $0.021\,\mathrm{N/m^2}$, which was lower than the previously estimated theoretical value of $0.035\,\mathrm{N/m^2}$ (refer to Eq. 42). Since the dissipation rate is directly proportional to the shear force, the actual dissipation rate is likely even smaller than our theoretical estimate. We can therefore conclude that the relative contribution of air damping during vibration was not significant. Given this conclusion, we did not extend the FLUENT analysis to 3D, as was done in the theoretical

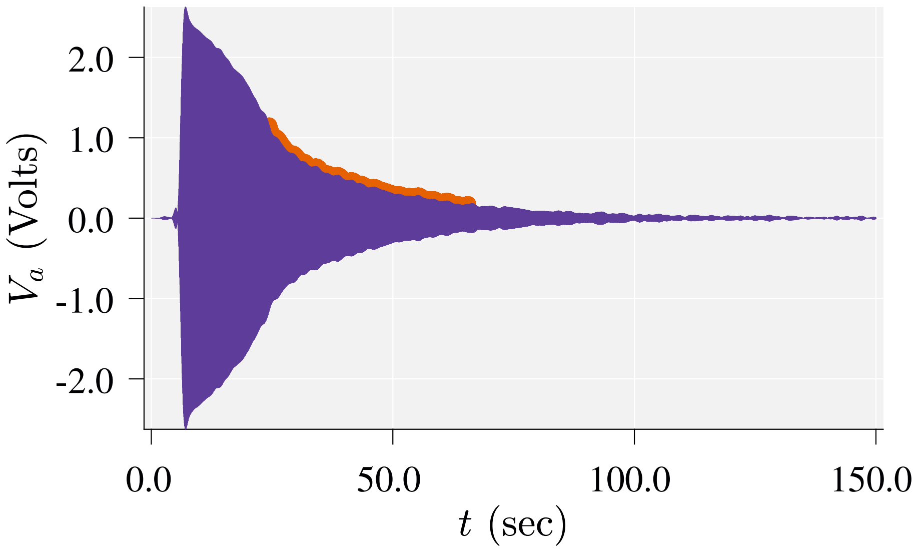

Figure 10: Atypical large-amplitude vibration data, observed less frequently. Despite the complexity of the large-amplitude behavior, the subsequent low-amplitude dynamics remained consistent with other low-amplitude vibrations.

analysis.

A final consideration is that knurling roughens the rod's surface, which could, in principle, increase air dissipation. The key question is: how much would air dissipation need to increase to account for the entire observed increase in overall dissipation? We emphasize that our goal is not to quantify the exact increase in internal damping but rather to assess whether a significant increase in internal damping could have occurred due to knurling.

Our theoretical estimate in Eq. (50) indicates that the coefficient of air damping is about 17 times smaller than the overall observed dissipation rate in plain rods (and the simulation results suggest it might be even smaller) as seen from Fig. 9. For example, if the original damping in the plain rods is taken as 100, then air damping would account for approximately 6. However, with knurling, the damping in the rods increased to 160 (as indicated by experimental data showing a 1.6-fold increase in the linear damping coefficient). Therefore, for air damping to be the primary contributor to this change, it would need to increase from 6 to 66, which is an increase by a factor of about 10.

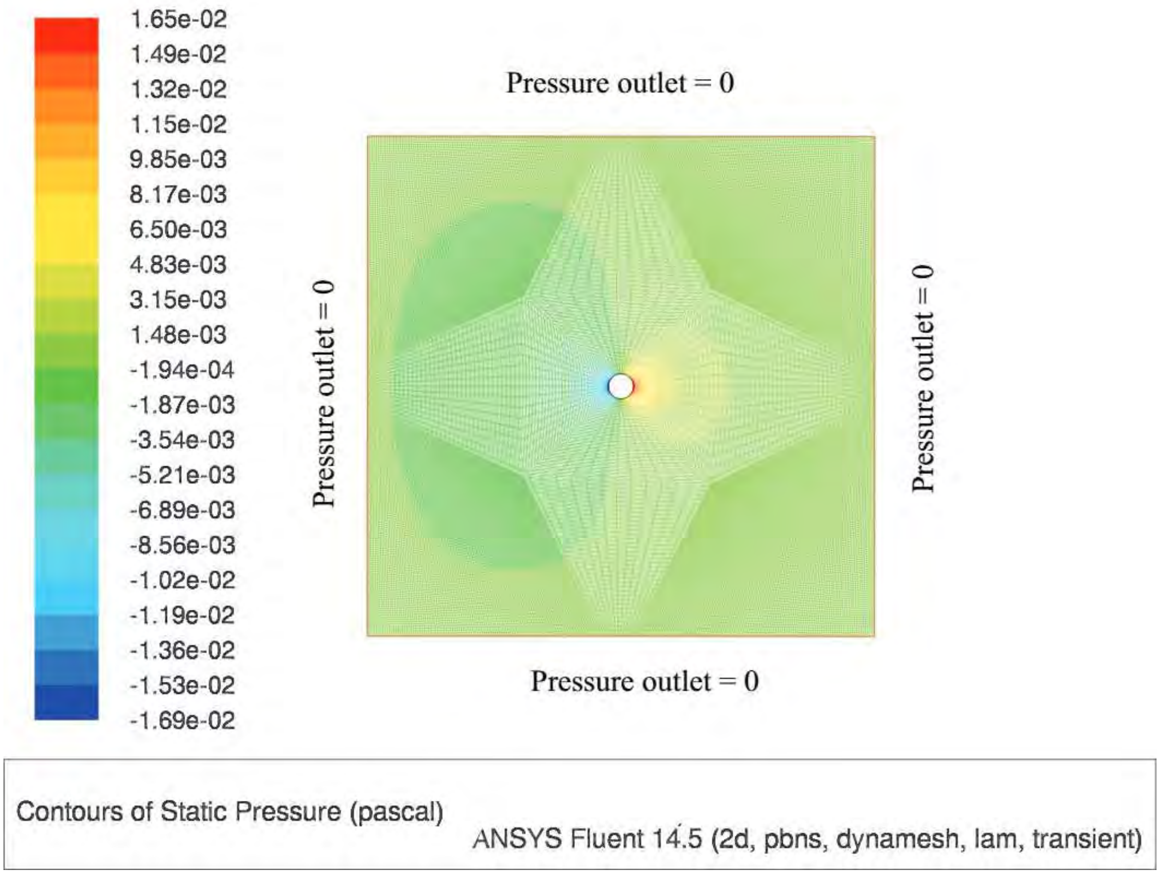

Figure 11: Two-dimensional FLUENT model used for simulating the oscillation of the rod. The rod was modeled as a bounded circular region with a radius equal to that of the rod, while air flowed in the surrounding square domain. The plot shows the contours of static pressure (Pascal) around the circular region resulting from the oscillation. A periodic velocity boundary condition (ω = 75 Hz, maximum displacement = 0.001 m) was applied to emulate the oscillation. The outlet pressure at the outer boundaries was set to zero.

To rule out the possibility of such a large increase in dissipation from the air, we simulated two-dimensional models of both smooth and knurled surfaces to explore the impact of surface texture on energy dissipation. Unlike previous simulations, where the cylinder oscillated, this setup held the circular geometries fixed while air flowed past them in the x-direction. The inlet air velocity was set to 0.1 m/s, which corresponds to a notional vibration amplitude of about 0.2 mm at 75 Hz, representing a small oscillation of the rod. By analyzing the steady-state pressure and velocity distributions at the inlet, we calculated the total energy (per unit length) entering the fluid domain for both surface types (plain and knurled). A higher energy value signifies a greater energy demand at the inlet, revealing that the system is dissipating more energy.

To validate our results, we analyzed energy dissipation across fluid domains of two different sizes, $30d \times 30d$ and $40d \times 40d$, where d is the diameter of the circle, to evaluate the convergence of dissipation values for *each* surface type. The results are presented in Table 3. Figures 12 and 13 illustrate two FLUENT simulation models corresponding to both surface types, for the $30d \times 30d$ domain.

Table 3: Energy dissipation rates for different fluid domain sizes.

Domain Size	Dissipation Rate (Plain) $\times 10^{-5}$ (W/m)	Dissipation Rate (Knurled) $\times 10^{-5}$ (W/m)
$30d \times 30d$	1.2974	1.5211
$40d \times 40d$	1.4022	1.4131

The results from Table 3 indicate that the dissipation values across different fluid domains do not vary significantly. While our goal is not to establish precise quantitative relationships, these findings clearly suggest that the surface roughness introduced by knurling does not increase air dissipation by an order of magnitude. Although this is a simplified simulation involving steady flow past a stationary rod, it is reasonable to infer that even for an oscillating rod, the increase in air damping due to knurling is *not* substantial.

Consequently, we conclude that the significant increase in damping observed for the knurled rods is attributable to changes in internal dissipation within the rods. These changes are likely caused by the extensive near-surface deformation resulting from knurling, which is consistent with previously reported increases in damping observed with techniques such as shot peening or sandblasting [6, 8, 9].

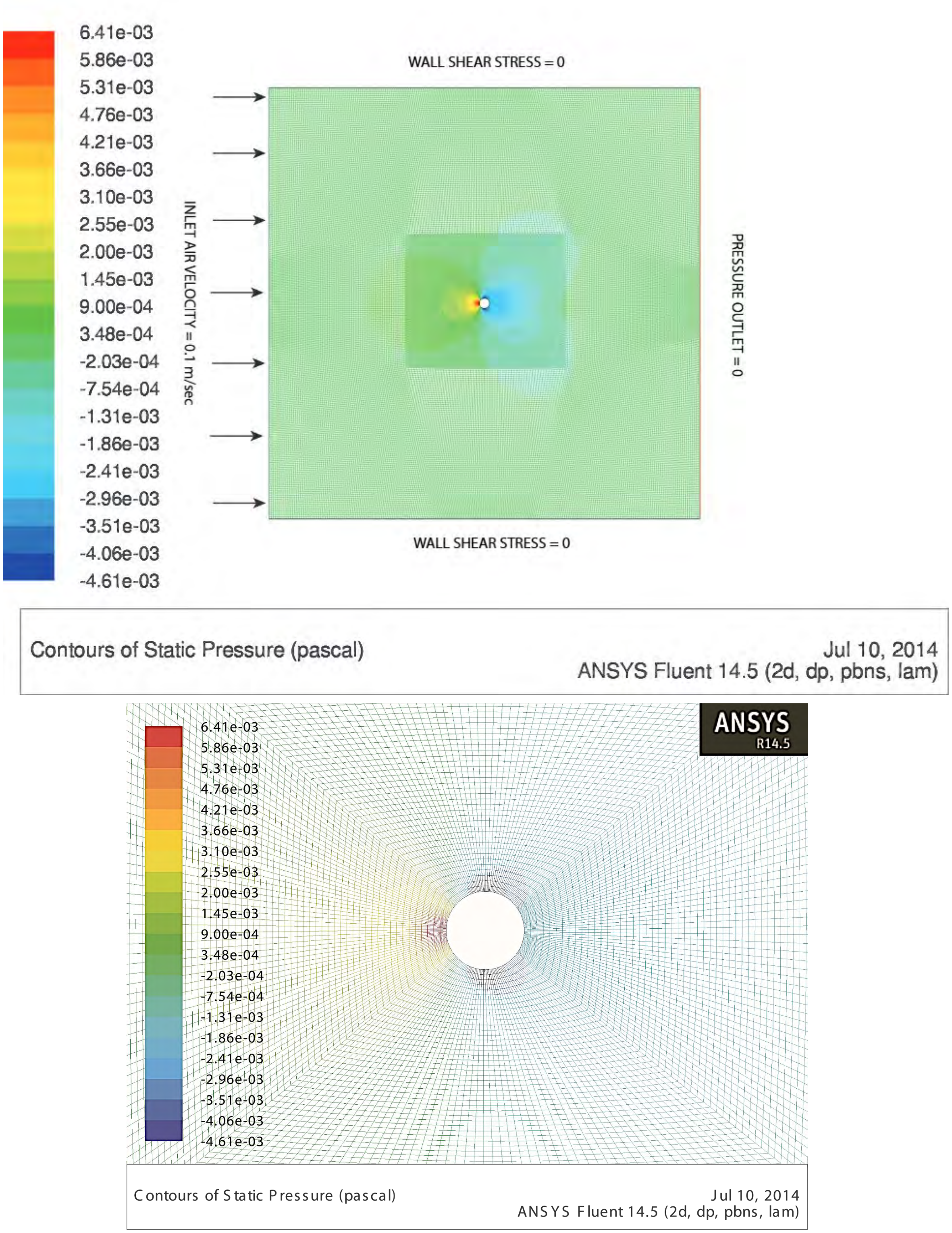

Figure 12: Plain circular geometry and the surrounding fluid domain in FLUENT. A zoomed-in view of the central region of the domain is shown in the plot at the bottom.

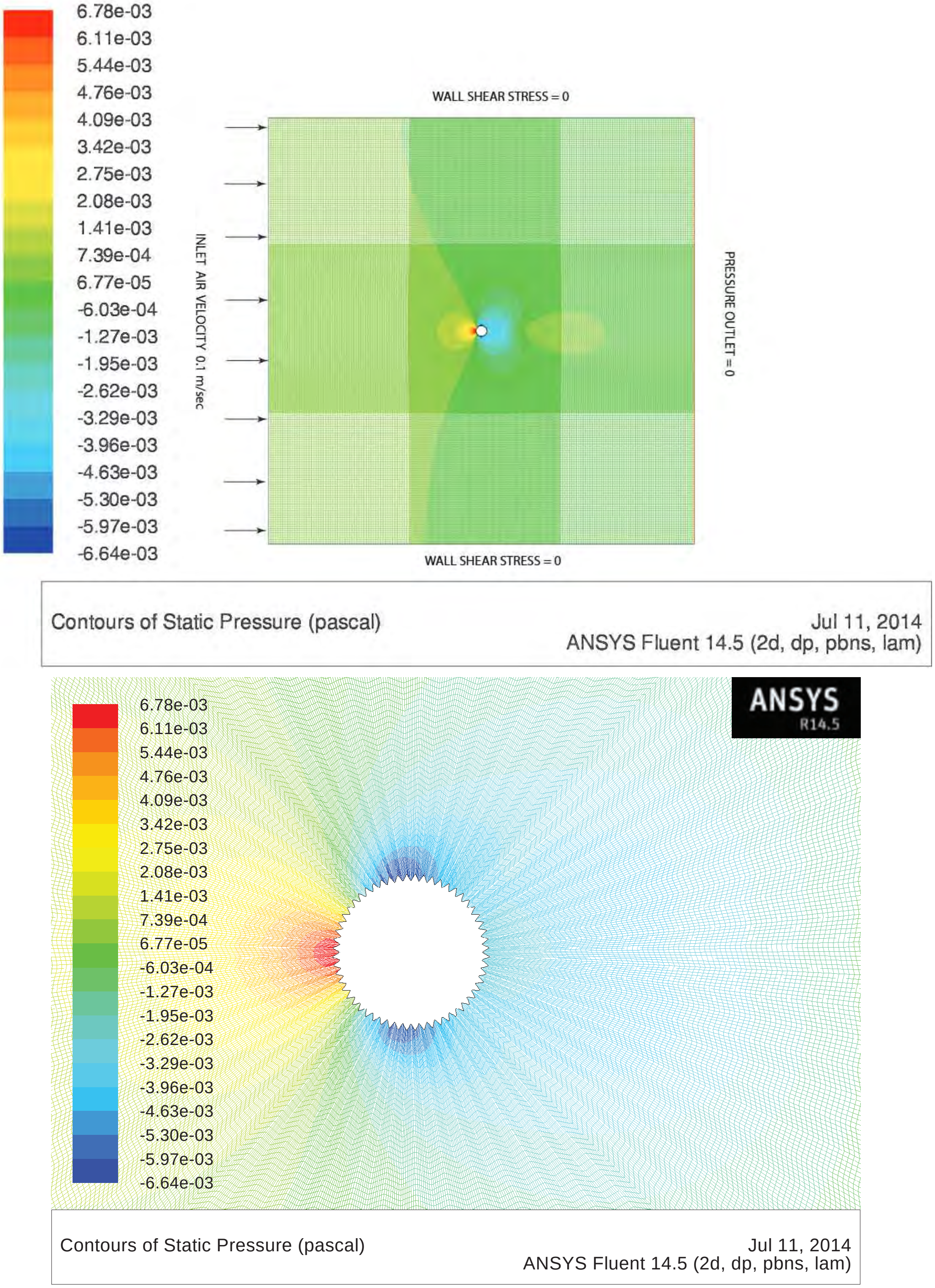

Figure 13: Circular knurled geometry and the surrounding fluid domain. As before, a zoomed-in view of the central region is shown at the bottom, which depicts the uneven surface representing the knurled surface.

5 Conclusions

The purpose of this research was to explore how surface deformation influences the damping characteristics of metal parts. To achieve this we investigated how knurling, a widely used surface modification technique, affects the damping in slender aluminum rods.

We first conducted experiments to observe the free oscillation of aluminum rods, both with and without surface alterations, to examine their damping characteristics. The damping coefficients for each type of rod were calculated and compared. Our findings were consistent, revealing that the damping coefficients of knurled rods were considerably higher than those of unaltered aluminum rods. Subsequently, we investigated whether the increased damping in knurled rods was attributable to air. Through an analytical study and FLUENT simulations, we estimated the air-induced dissipation levels in vibrations of both types of rods, concluding that air had a negligible impact on the damping of the rods.

Thus, we deduced that the enhanced damping was primarily due to increased internal damping within the material itself. Although this study did not directly examine how surface deformations like knurling affect internal damping, we derived some insights from the existing literature. Knurling, a process of plastic deformation, can introduce new dislocations, thus elevating the dislocation density within metals. The movement of these dislocations, either random or semi-random, during vibration, could heighten energy dissipation within the vibrating body. Although we presented theoretical calculations to rule out the conceivable role of air damping, our key contribution in this work is the empirical demonstration that a surface deformation process, such as knurling, serves as an effective means of enhancing damping in metal components. Future investigations may include detailed metallurgical analysis to examine the effects of varying metal types, post-knurling microstructural changes, and surface characterization to improve our understanding of surface deformation-induced damping in metals. Moreover, exploring hybrid approaches, such as combining surface-induced damping with viscoelastic coatings, may offer additional opportunities to improve damping performance. Such findings have potential applications in aerospace and automotive industries, where improved damping can mitigate unwanted resonance, reducing wear, noise, and structural damage, thus extending component life.

6 Acknowledgement

We thank Atanu Mohanty for providing theoretical and experimental guidance, particularly in air damping estimation and analog filter circuit development.

7 Author Disclaimer

This research was carried out while the first author was affiliated with the Indian Institute of Technology Kanpur.

References

[1] J. D. Eshelby. Dislocations as a cause of mechanical damping in metals. *Proceedings of the Royal Society of London. Series A, Mathematical and Physical Sciences*, 197(1050): 396–416, 1949.

[2] A. Granato and K. Lücke. Theory of Mechanical Damping Due to Dislocations. *Journal of Applied Physics*, 27(6):583–593, June 1956.

[3] W. De Silva Clarence. *Vibration Damping, Control, and Design.* Taylor & Francis, 2007.

[4] D. Nath S. S. Singh, P. K. Rohatgi and B. N. Keshavaram. Factors affecting the damping capacity of cast aluminium-matrix composites. *Journal of Materials Science*, 29(22):5975–5984, 1994.

[5] D. D. L. Chung. Review materials for vibration damping. *Journal of Materials Science*, 36(24):5733–5737, 2001.

[6] L. Singh R. A. Khan and M. L. Aggarwal. Relationship between damping factor and compressive residual stress for shot-peened austenitic stainless steel. *International Scholarly Research Network*, 2011:867484, 2011.

[7] H. L. Caswell. Investigation of low temperature internal friction. *Journal of Applied Physics*, 29(8):1210–1214, 1958.

[8] D. D. L. Chung and S. Wen. Enhancing the vibration reduction ability of concrete by using steel reinforcement and steel surface treatments. *Cement and Concrete Research*, 30(2):327–330, 2000.

[9] K. Venkateswara Reddy, R. Bheekya Naik, G. Madhusudhan Reddy, P. Chakravarthy, S. Janakiram, and R. Arockia Kumar. Damping capacity of aluminium surface layers developed through friction stir processing. *Materials Letters*, 298:130031, September 2021.

[10] Phalgun Nelaturu, Saumyadeep Jana, Rajiv S. Mishra, Glenn Grant, and Blair E. Carlson. Influence of friction stir processing on the room temperature fatigue cracking mechanisms of a356 aluminum alloy. *Materials Science and Engineering: A*, 716:165–178, 2018.

[11] E.H. Dowell. Damping in beams and plates due to slipping at the support boundaries. *Journal of Sound and Vibration*, 105(2):243–253, March 1986.

[12] N. Singer, W. Singhose, and W. Seering. Comparison of filtering methods for reducing residual vibration. *European Journal of Control*, 5(2–4):208–218, January 1999.

[13] Chunxu Qu, Guikai Tu, Fuzhong Gao, Li Sun, Shengshan Pan, and Dongsheng Chen. Review of bridge structure damping model and identification method. *Sustainability*, 16(21):9410, October 2024.

[14] J.E. Cooper. EXTENDING THE LOGARITHMIC DECREMENT METHOD TO ANALYSE TWO DEGREE OF FREEDOM TRANSIENT RESPONSES. *Mechanical Systems and Signal Processing*, 10(4):497–500, July 1996.

[15] Micah Allen, Davide Poggiali, Kirstie Whitaker, Tom Rhys Marshall, Jordy van Langen, and Rogier A. Kievit. Raincloud plots: a multi-platform tool for robust data visualization. *Wellcome Open Research*, 4:63, January 2021.

[16] Alireza Mojahed, Yang Liu, Lawrence A. Bergman, and Alexander F. Vakakis. Modal energy exchanges in an impulsively loaded beam with a geometrically nonlinear boundary condition: computation and experiment. *Nonlinear Dynamics*, 103(4):3443–3463, January 2021.

[17] K. Nandakumar and Anindya Chatterjee. Resonance, parameter estimation, and modal interactions in a strongly nonlinear benchtop oscillator. *Nonlinear Dynamics*, 40(2): 149–167, April 2005.

[18] M. S. Howe. *Acoustics of Fluid-Structure Interactions.* Cambridge University Press, Cambridge, 1st edition edition, August 1998.

[19] ANSYS Inc. *ANSYS Fluent User's Guide*, 2012. Version 14.5.

[20] L. Meirovitch. *Fundamentals of Vibrations.* McGraw-Hill Higher Education, 2002.

[21] L. B. Felsen and N. Marcuvitz. *Radiation and Scattering of Waves.* IEEE Press Series on Electromagnetic Wave Theory. Wiley, 1994.

[22] Milton Abramowitz and Irene A. Stegun. *Handbook of Mathematical Functions with Formulas, Graphs, and Mathematical Tables.* Dover Publications, New York, 1964.

A Calculation of natural frequency and mode shapes for free-free oscillation of the aluminum rods

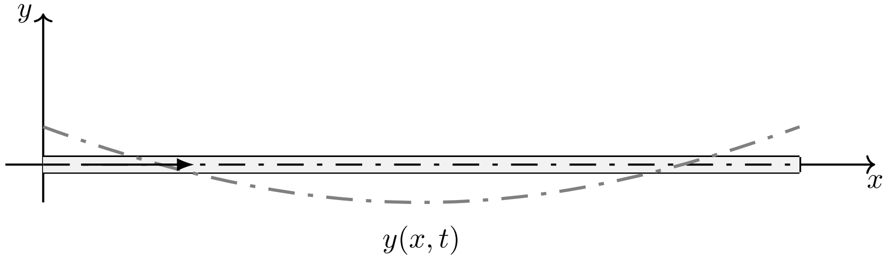

Figure 14: Schematic of a rod undergoing free-free oscillation. The transverse deflection is denoted by $y(x,t)$.

We present the method for calculating the natural frequency and mode shapes of the rods used in the experiment. The mechanical and geometric properties of the rod are as follows: Young's Modulus, $E = 70$ GPa; Mass per unit length, $m = 0.28$ kg/m; Area moment of inertia, $I = 8.5854 \times 10^{-10}\,\mathrm{m}^4$; and Length of the rod, $L = 834$ mm.

The governing equation for the transverse vibration of the rods is written as [20]:

$$-\left[EI(x)y''(x,t)\right]'' = m(x)\ddot{y}(x,t) \tag{5}$$

with boundary conditions:

$$EI(x)y''(0,t) = 0,\ EI(x)y'''(0,t) = 0,\ EI(x)y''(L,t) = 0,\ EI(x)y'''(L,t) = 0. \tag{6}$$

where prime denotes spatial and overdot indicates temporal derivative.

To solve Eq. (5), we assume a solution of the form $y(x,t) = Y(x)y(t)$ (using the method of separation of variables). This yields the following decoupled ODEs:

$$Y''''(x) - \beta^4 Y(x) = 0, \tag{7}$$

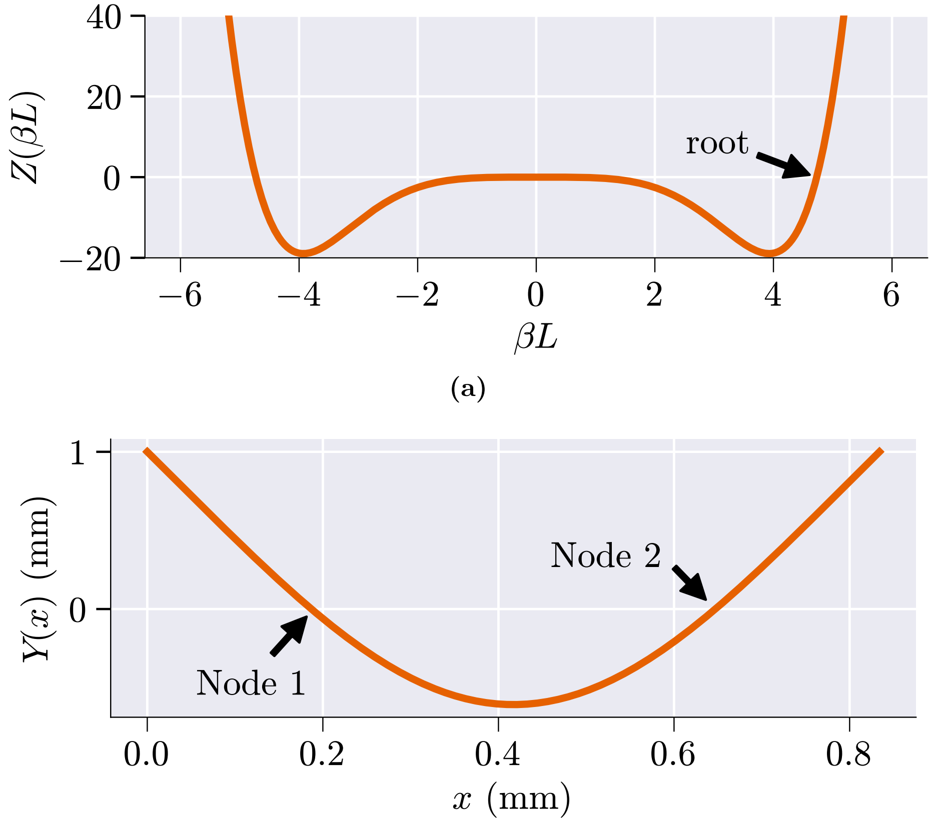

(a)

(b)

Figure 15: (a) Graphical estimation of the roots of the characteristic equation, $Z(\beta L) = \cos(\beta L)\cosh(\beta L) - 1$, for the free-free transverse oscillation of a rod. (b) The mode shape (Eq. 10) corresponding to the first vibration mode and the locations of its nodes.

$$\ddot{y}(t) + \omega^2 y(t) = 0. \tag{8}$$

where ω corresponds to the natural frequencies of the rod and β is given by

$$\beta = \sqrt[4]{\frac{\omega^2 m}{EI}}. \tag{9}$$

Solving Eq. (7) along with the boundary conditions, and substituting the values of E, I, L, and m we obtain:

$$Y(x) = \frac{1}{2}\left(-0.9825\,\sin(\beta x) - 0.9825\,\sinh(\beta x) + \cos(\beta x) + \cosh(\beta x)\right), \tag{10}$$

where the maximum tip displacement of the rod (at $x = 0$) is assumed to be 1 mm, and the characteristic equation:

$$\cos(\beta L)\cosh(\beta L) = 1 \tag{11}$$

We solved the characteristic equation graphically, as shown in Fig. 15a and obtained the solution corresponding to the first natural frequency, given by

$$\beta L = 4.73 \tag{12}$$

from which, the frequency ω was found to be 471.24 rad/sec (75 Hz) using Eqs. (9) and (12).

The nodes of the first mode shape were then calculated by solving $Y(x) = 0$ (refer to Eq. 10), which yielded: $x = 0.187$ and 0.647 within the interval $x \in (0, L = 0.834)$ as shown in Fig. 15b.

B Oscillation of an infinite plate in a viscous medium

For an infinite plate oscillating in the horizontal direction (refer to Fig. 16) in a medium, the governing equation can be written as:

$$\frac{\partial \vartheta}{\partial t} = \nu \frac{\partial^2 \vartheta}{\partial y^2}, \tag{13}$$

where

ϑ is the velocity of the medium,

ν is the kinematic viscosity of the medium.

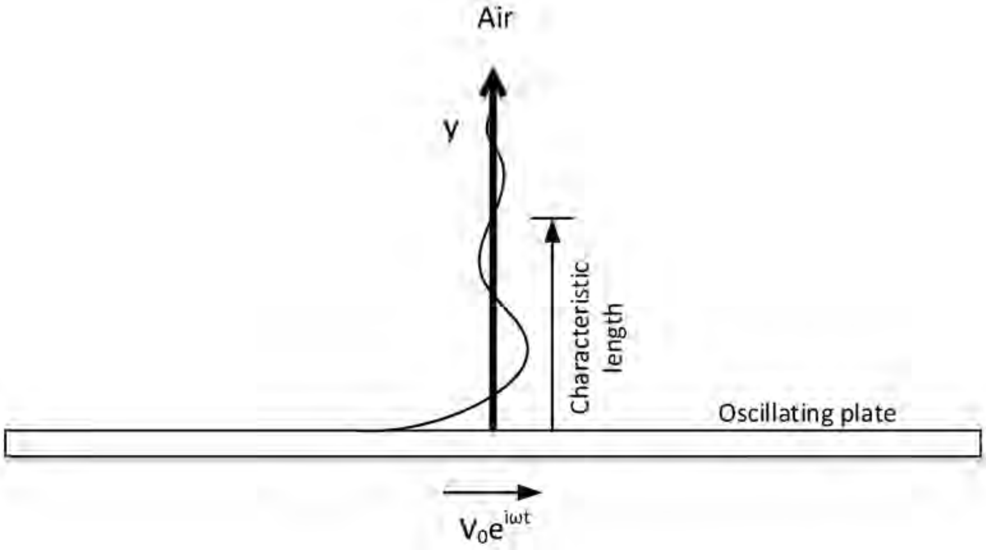

Figure 16: Schematic of an infinite plate oscillating in air with velocity amplitude V_0 and frequency ω.

Let the velocity of the plate be expressed as:

$$v = V_0 e^{i\omega t}. \tag{14}$$

The steady-state solution of Eq. (13) takes the form $\vartheta = U(y)e^{i\omega t}$. Substituting $\vartheta = U(y)e^{i\omega t}$ into Eq. (13), we obtain:

$$i\omega U(y) = \nu \frac{d^2U(y)}{dy^2} \tag{15}$$

Solving Eq. (15) and considering the decaying solution, we obtain:

$$\vartheta(y,t) = V_0 e^{-\sqrt{\frac{\omega}{\nu}}\frac{1}{\sqrt{2}}(1+i)y+i\omega t}, \tag{16}$$

or equivalently,

$$\vartheta(y,t) = V_0 e^{-\sqrt{\frac{\omega}{2\nu}}y+i\omega t}\left(\cos\left(\sqrt{\frac{\omega}{2\nu}}y\right) - i\sin\left(\sqrt{\frac{\omega}{2\nu}}y\right)\right) \tag{17}$$

Here, $y = \sqrt{\frac{2\nu}{\omega}}$, the characteristic length, provides a measure of the depth through which the viscous disturbance propagates into the medium. For the present case, this value was found to be 0.000257 m. As mentioned earlier, since this value is much smaller than the diameter of the oscillating cylinder in our problem, the solution obtained in Eq. (17) was used to estimate the viscous losses due to the oscillating cylinder in Appendix C.2.

C Analytical estimation of damping due to air

To estimate air damping for small oscillations, we assumed the fluid mechanics of the air to be linear. In this linearized framework, the response of the air includes an acoustic component, which arises from its compressibility, and a viscous component, owing to the inherent viscosity of the air.

C.1 Dissipation through acoustic radiation

For this analysis, we first determined the energy dissipation rate due to acoustic radiation from an infinitely long rigid cylinder oscillating in air. We initially derived a two-dimensional solution for the problem. Then, utilizing the known first mode shape of the oscillating rod, this two-dimensional solution was applied on a per-unit-length basis to estimate the dissipation rate for the actual rod. This estimate was then compared with the experimentally observed net dissipation, which revealed that the contribution of the acoustic effect was negligible. This outcome is not surprising, given that the rod's diameter is approximately 11.5 mm, while the vibration frequency of 75 Hz corresponds to a wavelength of about 5 m in air, which is much larger. Qualitatively, too, the sound produced by the vibrating rod was only faintly audible when the ear was placed within a few centimeters of the rod. Some details of the calculation are given below.

C.1.1 Pressure field

In Fig. 17a, we show a two-dimensional view of a rigid cylinder oscillating in air at a frequency ω. The displacement vector of the oscillating cylinder is assumed to have the form:

$$\mathbf{u} = U_0 e^{i\omega t}\,\hat{\mathbf{i}} \tag{18}$$

where U_0 denotes the maximum displacement; ω is the frequency of oscillation; and $\hat{\mathbf{i}}$ is unit vector along the horizontal direction.

The goal is to determine the pressure field p around the cylinder resulting from its oscillation. The governing equations are as follows [18, 21]:

$$\nabla^2 p - \frac{1}{c^2}\frac{\partial^2 p}{\partial t^2} = 0, \tag{19}$$

$$\frac{\nabla p}{\varrho_v} = -\frac{\partial v}{\partial t}, \tag{20}$$

where v and ϱ_v denote the velocity and the density of the medium, respectively, and c denotes the speed of sound in the medium. Assuming $p = p(\rho, \phi)e^{i\omega t}$ in polar coordinates, substitution into Eq. (19) yields:

$$\nabla^2 p + k^2 p = 0, \quad \text{where } k = \frac{\omega}{c}, \tag{21}$$

The solution to this Helmholtz wave equation in polar coordinates (see Fig. 17b) for an outward traveling wave is given by :

$$p = \sum_{m=0}^{\infty} H_m^{(2)}(k\rho)\left(C_m \cos(m\phi) + B_m \sin(m\phi)\right), \tag{22}$$

where m takes integer values. Here C_m and B_m are constants, and $H_m^{(2)}$ is the Hankel

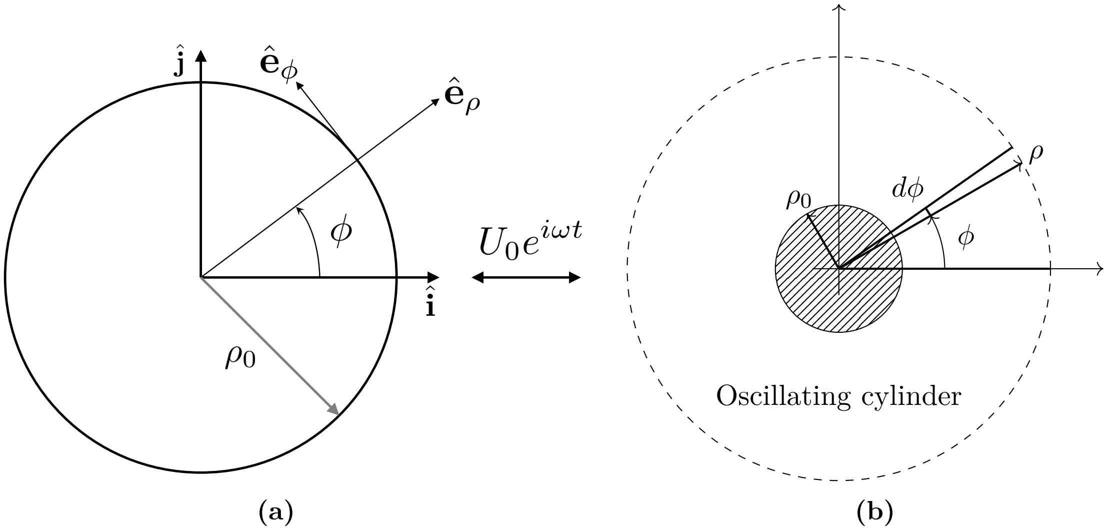

Figure 17: (a) Two-dimensional view of the rod oscillating in air with frequency ω, with a displacement given by $\mathbf{u} = U_0e^{i\omega t}\hat{\mathbf{i}}$. The unit vectors $\hat{\mathbf{e}}_\rho$ and $\hat{\mathbf{e}}_\phi$ denote the radial and tangential directions in polar coordinates, respectively (b) Closed circular loop of radius ρ used for line-integral in Eq. (29) to calculate acoustic energy dissipated from the oscillating cylinder per unit time per unit length.

function of the second kind [22]:

$$H_m^{(2)}(x) = J_m(x) - iY_m(x), \tag{23}$$

with $J_m(x)$ and $Y_m(x)$ being Bessel functions of the first and second kinds [22], respectively.

Now let us consider the velocity of the cylinder. On its boundary, the displacement ($\mathbf{u}$) and velocity ($\mathbf{V}$), in polar coordinates, can be written as:

$$\mathbf{u} = \left(U_0\cos(\phi)\hat{\mathbf{e}}_\rho - U_0\sin(\phi)\hat{\mathbf{e}}_\phi\right)e^{i\omega t}, \tag{24}$$

$$\mathbf{V} = i\omega\left(U_0\cos(\phi)\hat{\mathbf{e}}_\rho - U_0\sin(\phi)\hat{\mathbf{e}}_\phi\right)e^{i\omega t}. \tag{25}$$

Among the velocity components in the radial and tangential directions, we only considered the radial component, since the tangential component does not contribute to the acoustic effect. Furthermore, given that the radial component depends solely on $\cos(\phi)$, the resulting pressure field expression Eq. (22) then simplifies to:

$$p = H_1^{(2)}(k\rho)C_1\cos(\phi). \tag{26}$$

C.1.2 Velocity field

The velocity field of the air surrounding the oscillatory cylinder can also be written in the following form:

$$\mathbf{v} = \mathbf{v}(\rho,\phi)e^{i\omega t}. \tag{27}$$

Substituting $\mathbf{v}$ and p from Eqs. (26) and (27) respectively in Eq. (20), we obtain:

$$\mathbf{v}(\rho,\phi) = \frac{iC_1}{\omega\varrho_v}\left(kH_1'^{(2)}(k\rho)\cos(\phi)\hat{\mathbf{e}}_\rho - \frac{H_1^{(2)}(k\rho)\sin(\phi)}{\rho}\hat{\mathbf{e}}_\phi\right). \tag{28}$$

where

$$H_1'^{(2)}(x) = \frac{d}{dx}H_1^{(2)}(x) = \frac{d}{dx}(J_1(x) - iY_1(x)) = J_1'(x) - iY_1'(x)$$

Adopting a phasor approach to estimate the rate of energy dissipation per unit length we can write

$$q_{acoustic} = \frac{1}{2}\oint_{-\pi}^{\pi}\Re(p(\rho,\phi)(\hat{\mathbf{e}}_\rho\cdot\bar{\mathbf{v}}(\rho,\phi)))\rho d\phi \tag{29}$$

where the energy dissipation per unit length per unit time is denoted by q_{acoustic}; the amplitude of the time-varying pressure field is represented by $p(\rho,\phi)$; the complex conjugate of the amplitude of the velocity field is denoted by $\bar{\mathbf{v}}(\rho,\phi)$; and $\Re(\cdot)$ denotes the real part of $(\cdot)$. Equation (29) represents the energy dissipated from the oscillating cylinder per unit time per unit length through any closed circular domain lying at a distance ρ ($\rho > \rho_0$, the radius of the cylinder) from the center of the oscillating cylinder (refer to Fig. 17b). Note that we only considered the *radial component* of the velocity field for the analysis.

Substituting the values of pressure and velocity from Eqs. (26) and (28) respectively in Eq. (29), we obtain:

$$\begin{aligned} q_{\text{acoustic}} &= \oint_{-\pi}^{\pi} \Re\left(\frac{kC_1\bar{C}_1 \cos^2(\Phi)(J_1(k\rho) - iY_1(k\rho))(Y_1'(k\rho) - iJ_1'(k\rho))}{2\omega\varrho_v} \right) \rho d\phi \\ &= \oint_{-\pi}^{\pi} \frac{k\left|C_1\right|^2 \cos^2(\Phi)(Y_1'(k\rho)J_1(k\rho) - J_1'(k\rho)Y_1(k\rho))}{2\omega\varrho_v} \rho d\phi \end{aligned}$$

Using the relation $(Y_1'(k\rho)J_1(k\rho) - J_1'(k\rho)Y_1(k\rho)) = \frac{2}{\pi k\rho}$, we can write,

$$\begin{aligned} q_{\text{acoustic}} &= \oint_{-\pi}^{\pi} \frac{k\left|C_1\right|^2 \cos^2(\Phi)\left(\frac{2}{\pi k\rho}\right)}{2\omega\varrho_v} \rho d\phi \\ &= \frac{\left|C_1\right|^2}{\omega\varrho_v} \end{aligned} \tag{30}$$

To determine C_1, we impose the velocity boundary condition. On the boundary of the oscillating cylinder, the radial components of the air and cylinder velocities are the same. From Eqs. (25) and (28), equating the radial components at $\rho = \rho_0$, we obtain:

$$U_0 \cos(\phi) i\omega = \frac{iC_1}{\omega\varrho_v} k H_1'^{(2)}(k\rho)\cos(\phi) \tag{31}$$

From the above equation, we obtain

$$C_1 = \frac{U_0\omega^2\varrho_v}{kH_1'^{(2)}(k\rho_0)} \tag{32}$$

Putting $\varrho_v = 1.1644\,\text{kg/m}^3$, $\omega = 471\,\text{rad/sec}$, $k = 1.3491\,\text{rad/m}$, and $\rho_0 = 0.00575\,\text{m}$ in Eqs. (30) and (32) we obtain:

$$q_{\text{acoustic}} = -0.596U_0^2. \tag{33}$$

Now for the actual rod the value of U_0 varies with the length of the rod. This variation is dependent on the shape function of the mode $(\Phi(x))$ in which the rod vibrates. We can write,

$$U_0(x) = U_0\Phi(x). \tag{34}$$

and,

$$q_{acoustic}(x) = -0.596U_0^2\Phi^2(x). \tag{35}$$

The losses from the above expression can be integrated over the length of the rod to obtain an estimate of the net dissipation. Thus:

$$Q_{acoustic} = -0.596U_0^2\int_0^L \Phi(x)^2dx. \tag{36}$$

where $U_0\phi(x)$ is the shape function corresponding to the first mode of vibration with maximum amplitude U_0. $Q_{acoustic}$ is the energy lost per unit time from the aluminum rod in air during oscillation.

Let us now consider the rate of change in the *kinetic energy* of the oscillating rod, which can be written as:

$$\dot{E} = \frac{\omega^2 mU_0\dot{U}_0}{L}\int_0^L \Phi(x)^2dx. \tag{37}$$

We note that U_0 is not a constant quantity, and *decays slowly with time* which allows us to speak of its slow average rate of change.

Equating $\dot{E}$ with $Q_{acoustic}$ using Eqs. (36) and (37) we obtain:

$$\dot{U}_0 = \frac{-0.596U_0L}{m\omega^2}. \tag{38}$$

Substituting m/L =0.24 kg/m, and $\omega = 471$ rad/sec we obtain:

$$\dot{U}_0 = -9.5865\times 10^{-6}U_0. \tag{39}$$

Comparing Eqs. (3) and (39) (note that U_0 and A are equivalent) we see that the rate of amplitude decay in Eq. (39) is much lower than the linear damping coefficient value $a_2 = 0.0395$ (plain rods) obtained experimentally, as shown in Fig. 9a. Hence, we conclude that the energy dissipation through acoustic radiation in the surrounding air has negligible contribution in damping of the aluminum rods.

C.2 Viscous dissipation

To estimate the viscous dissipation due to air near the oscillating cylinder, we solved for the motion of the fluid, and treated the velocity condition as given on the boundary of the rod. However, unlike the analysis of the acoustic part where only the radial component of the velocity was considered, the viscous effect was determined by considering the tangential velocity component of the oscillating cylinder.

This problem was further approximated by considering an infinite plate oscillating with frequency ω in contact with a viscous fluid. In this case, we found the characteristic length, which represents the distance over which the amplitude decreases by a factor of e, indicating the depth to which the disturbance penetrated the fluid was approximately 0.257 mm (refer to Appendix B for detailed analysis). Since this was rather small compared to the diameter of the rod (roughly 2% of 11.5 mm) it was concluded that an order of magnitude estimation of the damping could be obtained by using the planar solution, and integrating it over the perimeter of the cylinder.

Recalling Eq. (16), the velocity of the fluid surrounding the oscillating plate is written as

$$\vartheta(y,t) = V_0 e^{-\sqrt{\frac{\omega}{2\nu}}(1+i)y + i\omega t} \tag{40}$$

where ϑ indicates the velocity of the medium, ν is the kinematic viscosity of the medium, and V_0 and ω represent the amplitude and frequency, respectively, of the velocity of the oscillating plate.

Now, for the actual problem (see Figs. 17a and 18) $V_0 = \omega U_0 \sin(\phi)$ since for viscous dissipation only the tangential velocity component of the cylinder is considered. Then ϑ is written as

$$\vartheta(y, \phi, t) = \omega U_0 \sin(\phi) e^{-y\sqrt{\frac{\omega}{2\nu}}(1+i)+i\omega t} \tag{41}$$

The rate of energy dissipation was obtained by calculating the dissipation rate *at the boundary* of the cylinder due to the engendered shear force (τ) inside the medium given by

$$\begin{aligned} \tau(y=0, \phi, t) &= \mu \left(\frac{\partial \vartheta}{\partial y}\right)\Big|_{y=0} \\ &= \mu\omega U_0 \sin(\phi) \left(-\sqrt{\frac{\omega}{2\nu}}\right)(1+i) e^{-\sqrt{\frac{\omega}{2\nu}}(1+i)y+i\omega t}\Big|_{y=0} \\ &= \mu\omega U_0 \sin(\phi) \left(-\sqrt{\frac{\omega}{2\nu}}(1+i)\right) e^{i\omega t}. \end{aligned} \tag{42}$$

Following a similar methodology used in the previous section, we estimated the dissipation rate per unit length as

$$q_{viscous} = \frac{1}{2}\oint_{-\pi}^{\pi} \Re\left(|\tau(y=0,\phi)|\,|\bar{\vartheta}(y=0,\phi)|\right)\rho_0 d\phi \tag{43}$$

where $|(\cdot)|$ indicates the amplitude of $(\cdot)$, and $\bar{\vartheta}$ denotes the complex conjugate of ϑ.

From Eqs. (41) to (43) the rate of energy dissipation per unit length can be written as:

$$q_{\text{viscous}} = -U_0^2\omega^2\rho_0\pi\sqrt{\frac{\mu\omega\varrho_v}{8}}. \tag{44}$$

Putting $\varrho_v = 1.1644$ kg/m^3, $\omega = 471$ rad/sec, $k = 1.3491$ rad/m, and $\mu = 1.983 \times 10^{-5}$ Kg/ms in Eq. (44) we get:

$$q_{\text{viscous}} = -6.6620 \times 10^{-4} U_0^2\omega^2. \tag{45}$$

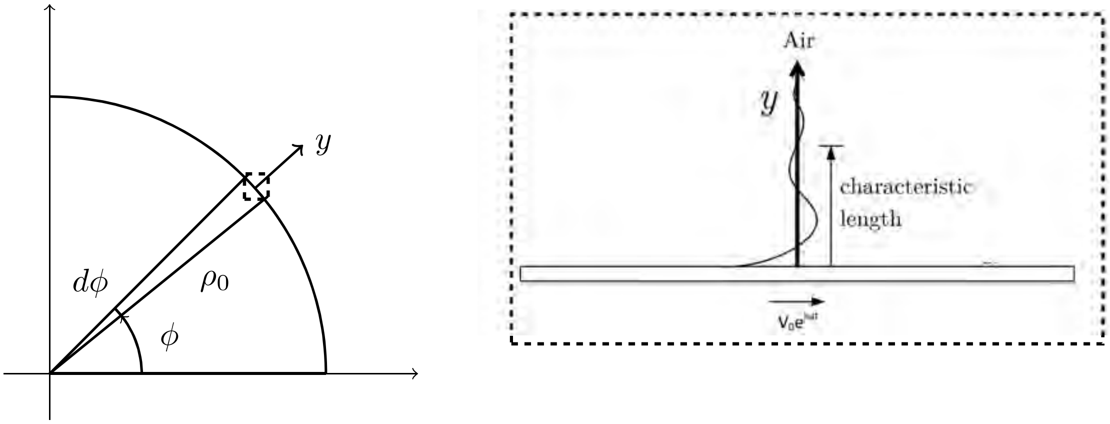

Figure 18: The solutions of the oscillating plate problem (see Appendix B) was used for estimating the viscous losses due to the oscillating cylinder.

Now following Eq. (34), and Eq. (35) for this case also we can write,

$$q_{\text{viscous}}(x) = -6.6620 \times 10^{-4} U_0^2(x)\omega^2. \tag{46}$$

$U_0(x)$ is the same as before.

The rate of energy dissipation of the entire rod can then be found as

$$Q_{viscous} = \int_0^L q_{viscous}(x)dx. \tag{47}$$

or,

$$Q_{viscous} = -6.6620 \times 10^{-4} U_0^2 \omega^2 \int_0^L \Phi^2(x)dx. \tag{48}$$

$Q_{viscous}$ is the energy lost due to viscous effect per unit time from the aluminum rod in air during vibration. Again considering the rate of change in the *kinetic energy* of the oscillating rod from Eq. (37), and comparing it with Eq. (48) we obtain:

$$\dot{U}_0 = \frac{-6.6620 \times 10^{-4} U_0 L}{m}. \tag{49}$$

Substituting $m/L = 0.24$ kg/m we get:

$$\dot{U}_0 = -0.0023U_0. \tag{50}$$

This shows that the linear damping coefficient (coefficient of U_0) is almost 17 times smaller than the value $a_2 = 0.0395$ (plain rods), observed from the experimental results shown in Fig. 9a.